

# GUIDED WAVE INTERPRETATION FOR INTEGRATED VEHICLE HEALTH MANAGEMENT SENSORS

Jill Bingham  
Nondestructive Evaluation Laboratory  
Department of Applied Science  
The College of William and Mary

## **Abstract**

Integrated Vehicle Health Management (IVHM) combines the use of onboard sensors with artificial intelligence algorithms to automatically identify and monitor structural health issues. A fully integrated approach to IVHM systems demands an understanding of the sensor output relative to the structure, along with sophisticated prognostic systems that automatically draw conclusions about structural integrity issues. Ultrasonic guided wave methods allow us to examine the interaction of multiphysics signals within key structural components. Since they propagate relatively long distances within plate- and shell-like structures, guided waves allow inspection of greater areas with fewer sensors. We have developed parallel processing, 3D elastic wave simulations using the finite integration technique in order to systematically examine the wave propagation in structures. Interpreting the simulated and experimental signals that we receive from transducers we look not only at the wave mechanics but also the signal processing using the dynamic wavelet fingerprinting technique to deliver the information in a form that does not require extensive knowledge of the guided wave physics.

## **Introduction**

With a national fleet of aging aircraft and infrastructure, safety will become an increasing priority. IVHM promises low-cost, real-time sensing/inspection methods to detect damage before catastrophic failure. Ultrasonic guided waves, Lamb waves, allow for large areas of plate-like structures, such as airframes, storage tanks and pipes to be

inspected with fewer sensors than conventional point by point measurements since they interrogate the entire region between sensor pairs<sup>1234</sup>. By understanding the waveguide physics we can develop systems that are tailored to the application at hand. However due to the complicated nature of guided wave propagation, we also develop algorithms that automatically analyze the waveforms and present the critical information in a form that doesn't require users to have extensive knowledge of the physics. The propagation of the Lamb wave modes depends on the transducer excitation frequency along with the thickness and material properties of the structure. So variations in the waveforms can be used to assess the integrity of the structure for flaws such as disbonds, corrosion and cracks that represent changes in effective thickness and/or local material properties.

The research presented in this paper deals with our efforts to understand the wave propagation in airframe stringers and their interaction with corrosion and thickness loss flaws. First using an incremental thickness loss experiment and an accelerated corrosion test, we look at the changes at the in mode arrivals. In each case we employ the dynamic wavelet fingerprinting technique (DWFT) to extract mode arrivals<sup>5</sup>. Then we developed a 3D elastic wave finite integration simulation to model the waves in the structure.

## **Experimental Details**

In order to reduce the weight of an aircraft, we can use sensors to track structural integrity instead of engineering redundancy into the structure. Some of the structural

pieces of interest are the airframe stringers. This set of studies was conducted on sample aluminum stringers that are 1m in length and have a “T” cross-section. The original flange thickness was 1.6mm. We use piezoelectric contact transducers in a pitch-catch arrangement to inspect the samples. The transmitting transducer excites Lamb wave modes that are then recorded by the receiving transducers. Since the Lamb wave modes are dispersive, the presence of a flaw shifts the arrival times and amplitudes of the Lamb wave modes received. Figure 1 shows the dispersion curves for Lamb waves in aluminum, depicting how a change in the thickness of the material results in a change in the group velocity of the mode.

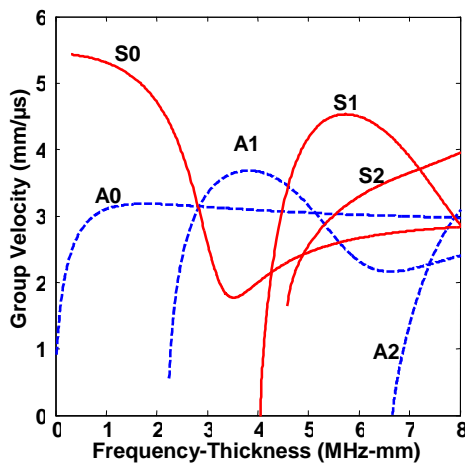


Figure 1: Lamb wave dispersion curves for an aluminum plate. A change in thickness of the material results in a change in arrival time of the mode since its group velocity changes.

By exciting the transducers at lower frequencies we ensure that the frequency thickness product is below the cut-off frequencies for the higher modes, making the waveforms less complicated. In the instance of the 1.6mm thick aluminum stringer, this means using excitation frequencies of 1.4 MHz or lower. In this region of the dispersion curve any thickness loss will be represented as a increase in the group velocity of the first arriving, S0 mode, while the second mode, the

A0 mode will have a relatively small change in arrival over the same change in thickness.

### **Dynamic Wavelet Fingerprinting Technique (DWFT)**

Due to the need to extract multiple mode arrivals from the complicated time-series data received by the transducers, we have found that joint time-frequency methods are commonly used<sup>6</sup>. They have the ability to isolate individual spectral components while retaining their absolute relationships in the time domain. Specifically, we have found that using the wide versatility of wavelet transformations is perfect for this application. By choosing a mother wavelet that optimally represents a signal feature, i.e. a mode, we can better isolate features of interest in time-scale representation. Another added bonus to this approach is that the transformation takes the 1D signal and transforms it into a 2D image that allows us to work with 2D image processing operations. Our DWFT renders the time-series signal as binary contour plots of the wavelet transform coefficients. The resulting fingerprint-like image is amenable to computerized interpretation for automated extraction of signal features of interest.

Figure 2 illustrates how the wavelet fingerprints are formed. An isolated ultrasonic pulse is shown in (a) along with a standard surface plot (b) of the corresponding continuous wavelet coefficients. In (b) we also see the coefficients displayed as a traditional contour plot underneath the surface plot. To form a wavelet fingerprint, we use the “thick contours” shown in (c). The wavelet coefficients are first normalized into the range of [0, 1], and then equal slices of the 3D-coefficient surface are projected back onto the time-scale plane. This results in the black and white, 2D representation shown in (d) which we refer to as the wavelet fingerprint. The wavelet fingerprint is then amenable to image recognition algorithms that automatically pull out the features of interest.

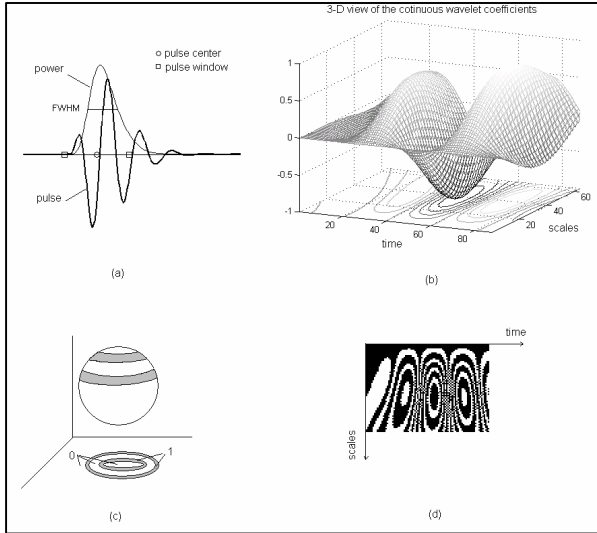


Figure 2: Wavelet fingerprints generation. (a) Ultrasound pulse; (b) 3D view of the wavelet coefficients and its contour; (c) slice projection; (d) the dynamic wavelet fingerprint of (b).

## Results and Discussion

### **Incremental Thickness Milling**

We began investigating the interaction of the guided waves with the stringers by simulating the effect of corrosion. By incrementally decreasing the thickness of the stringer flange with a milling machine, we know precisely how much material we are removing at each step. The clean T-stringer is 1m long and the bottom flange is 20mm wide on each side of the web. So sitting on the table it looks like an upside down “T”. The milling increments were taken from the middle 40cm of the bottom flange. Figure 3 shows the thickness versus milling step.

For the tests the transducers were placed 10cm from the ends of the stringers again in an effort to separate the reflections from the ends out in time from the signal that we care about. So the total propagation length was 80cm with the flaw in the middle. The raw waveforms collected with the catch transducer were passed through a discrete stationary wavelet filter removing a couple of layers of detail. A windowed portion of this filtered signal was then passed to the DWFT

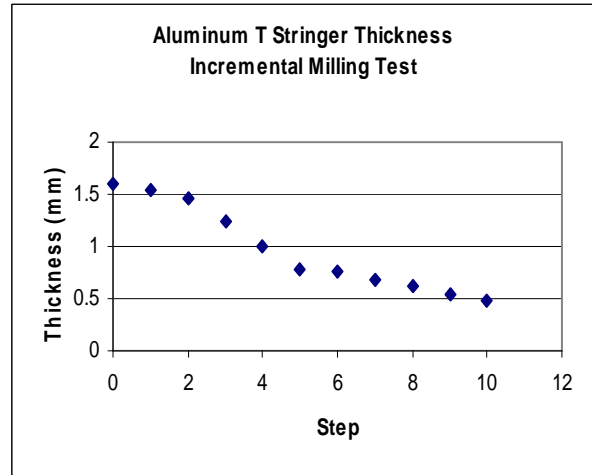


Figure 3: Incremental milling steps.

algorithm to find the fingerprints. The window was determined using the expected arrival time for the first arriving  $S_0$  mode. Figure 4 shows the binary fingerprint images produced from the incremental milling tests. The top image is for the un-milled clean sample. The feature of interest is located towards the right. The red and blue lines are included for visual reference. As material is removed from the flange, we would expect from the dispersion curves that the  $S_0$  mode would speed up. In these images a speed up of the mode would mean a sooner arrival time and a shift of the feature to the left. It can be seen in the images, the feature shifts left towards the blue line. Furthermore there seems to be a split in the feature with part of it remaining at the original location, this could be from some of the guided wave energy passing through the fully intact side of the stringer unchanged.

Now that we have a good indicator of the change in mode velocity and arrival time we can look at our accelerated corrosion tests to find similar trends.

### **Accelerated Corrosion Test**

In order to study the interaction between the guided waves and a more real world sample we set up an accelerated corrosion test in which we introduced

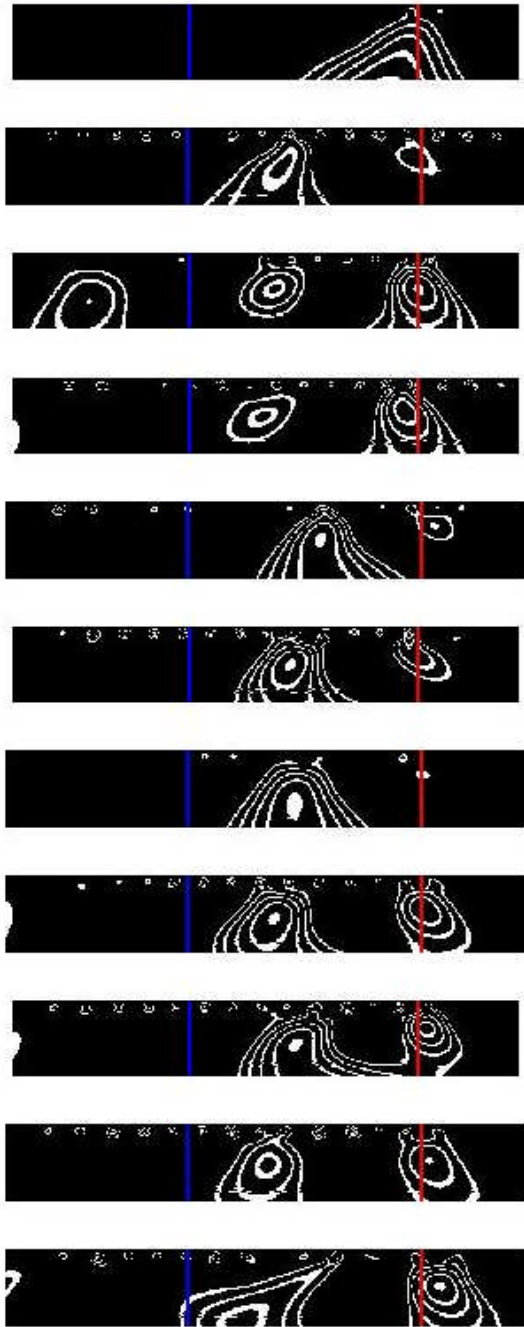


Figure 4: DWFT generated finger prints for the windowed, filtered waveforms of the S0 modes for the incremental milling test. The red and blue lines give visual reference to show how the feature moves to the left indicating a sooner arrival time.

corrosion on a portion of the surface of the flange on the stringer. The accelerated corrosion test came from an ASTM standard test method known as the EXCO test<sup>7</sup>. The

EXCO solution produced an exfoliation form of corrosion which flaked off layers of the exposed surface. Figure 5 shows a close up of the final extent of the accelerated corrosion tests.

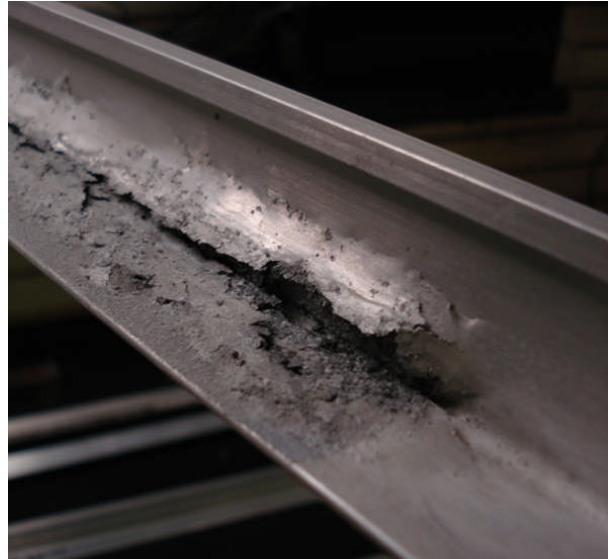


Figure 5: Close up of exfoliation corrosion on the stringer flange.

The excitation and treatment of the data were the same as for the milling tests. The contact transducers were placed 10cm from each of the ends of the 1m “T” stringer. The middle 40cm of the flange was exposed to the EXCO solution.

The raw waveforms from the accelerated corrosion tests were much more noisy and complex than from the incremental milling tests. This is because of the nature of the exfoliation; each of the flakes becomes a scatterer of the elastic wave energy.

Figure 6 shows the results from processing the accelerated corrosion data. Again, the feature moves from the right, left towards the blue line. The shift in this set of data is more subtle because as the EXCO solution eats away at the stringer, the material properties and thickness don’t change in a stepwise function as they did with the milling samples.

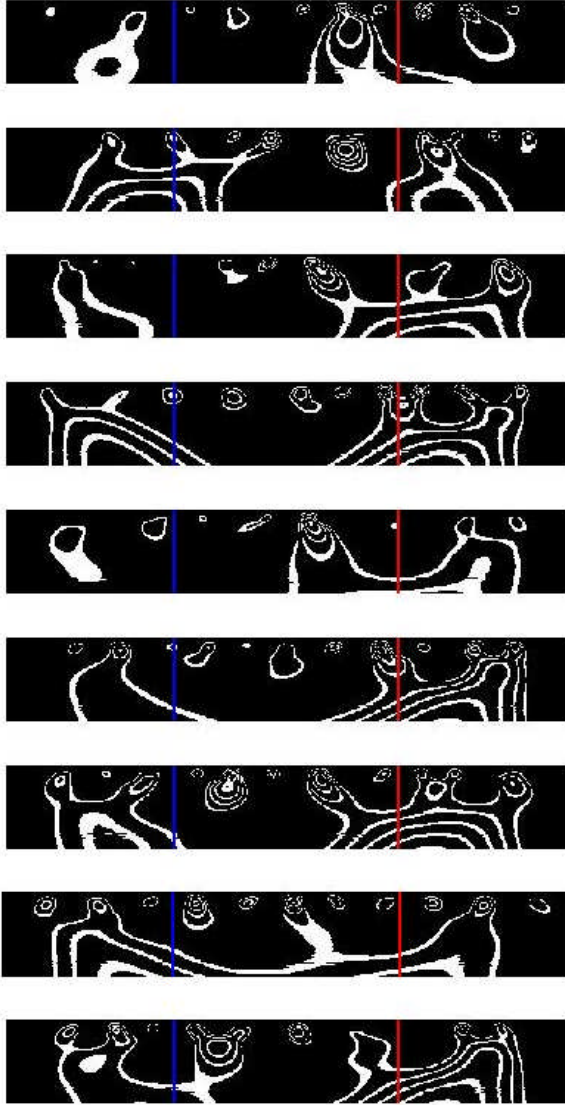


Figure 6: DWFT images from the EXCO accelerated corrosion tests. Red and blue lines included for reference to help identify feature that shifts from right to left indicating a sooner arrival time and thinning of stringer.

### Elastodynamic Finite Integration Technique (EFIT)

In order to further understand the interaction of the guided waves with the corroding airframe stringers we needed a way to model the waves in three dimensional structures. The dispersion curves are good indicators for plate-like conditions but the stringers are extruded “T” cross-section structures. We have developed a 3D

simulation technique that can take these features into account.

The finite integration technique stems from the basic equations of waves in solids. In total we have 9 equations to deal with. Three for the velocity components from Cauchy’s equation:

$$\rho \dot{v}_x = \frac{\partial T_{xx}}{\partial x} + \frac{\partial T_{xy}}{\partial y} + \frac{\partial T_{xz}}{\partial z} + f_x$$

$$\rho \dot{v}_y = \frac{\partial T_{xy}}{\partial x} + \frac{\partial T_{yy}}{\partial y} + \frac{\partial T_{yz}}{\partial z} + f_y$$

$$\rho \dot{v}_z = \frac{\partial T_{xz}}{\partial x} + \frac{\partial T_{yz}}{\partial y} + \frac{\partial T_{zz}}{\partial z} + f_z$$

Hook’s law gives the six unique components of the stress tensor:

$$\dot{T}_{xx} = (\lambda + 2\mu) \left( \frac{\partial v_x}{\partial x} \right) + \lambda \left( \frac{\partial v_y}{\partial y} + \frac{\partial v_z}{\partial z} \right)$$

$$\dot{T}_{yy} = (\lambda + 2\mu) \left( \frac{\partial v_y}{\partial y} \right) + \lambda \left( \frac{\partial v_x}{\partial x} + \frac{\partial v_z}{\partial z} \right)$$

$$\dot{T}_{zz} = (\lambda + 2\mu) \left( \frac{\partial v_z}{\partial z} \right) + \lambda \left( \frac{\partial v_x}{\partial x} + \frac{\partial v_y}{\partial y} \right)$$

$$\dot{T}_{xy} = \mu \left( \frac{\partial v_y}{\partial x} + \frac{\partial v_x}{\partial y} \right)$$

$$\dot{T}_{xz} = \mu \left( \frac{\partial v_z}{\partial x} + \frac{\partial v_x}{\partial z} \right)$$

$$\dot{T}_{yz} = \mu \left( \frac{\partial v_z}{\partial y} + \frac{\partial v_y}{\partial z} \right)$$

Each of these equations is discretized and the components are placed on a staggered grid.<sup>8,9,10</sup> This staggered grid allows for second order accuracy with first order discretization. Figure 7 shows the unit cell for the discretized grid that we use to build up the 3D structures. The red dots and arrows indicate components that are for the current cell while the blue dots and arrows show the locations of the components in neighboring cells that help update and define the current cell.

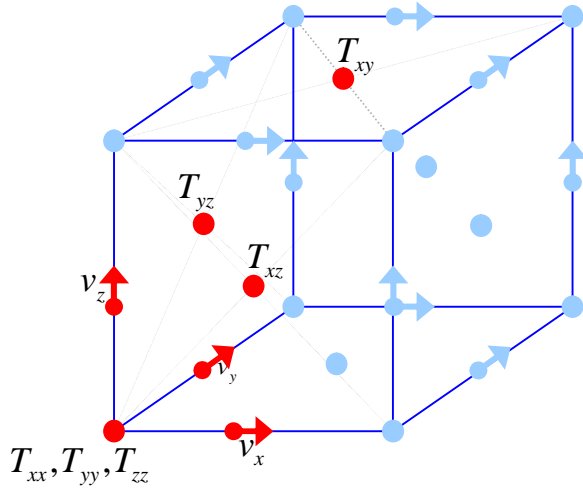


Figure 7: Unit cell for EFIT 3D simulation. Red dots and arrows indicate location of component for current cell, the blue dots and arrows are for neighboring cells.

Temporal discretization allows for the elastic wave calculation to be performed solely in the time domain. First we update the velocity components then in the next half time-step update the stress components.

$$v_i^{[k]} = v_i^{[k-1]} + v_i^{[k-1/2]} \Delta t$$

$$T_{ij}^{[k+1/2]} = T_{ij}^{[k-1/2]} + \dot{T}_{ij}^{[k]} \Delta t$$

The time-step and grid size are driven by the Courant-Friedrichs-Levy Criterion:

$$\Delta t \leq \frac{1}{c_{\max} \sqrt{1/(\Delta x)^2 + 1/(\Delta y)^2 + 1/(\Delta z)^2}}$$

$$\Delta x, \Delta y, \Delta z \leq \frac{1}{8} \lambda_{\min} = \frac{1}{8} \frac{c_{\min}}{f_{\max}} \approx \frac{1}{10} \frac{c_{s,\min}}{f_{\max}}$$

The grid size has to be less than one eighth of the smallest wavelength in order to have the accurate resolution. With all of the components determined all that is left to do is to apply the stress-free boundary conditions and update the cells by stepping through time.

Because of the small grid size needed we end up creating huge arrays of numbers that overwhelm typical desktop CPU's. We have parallelized the code to run on multiple computers to alleviate memory storage problems. Figure 8 shows an image of a simulated guided wave traveling down the

length of an aluminum plate the dimensions of the stringer flange.

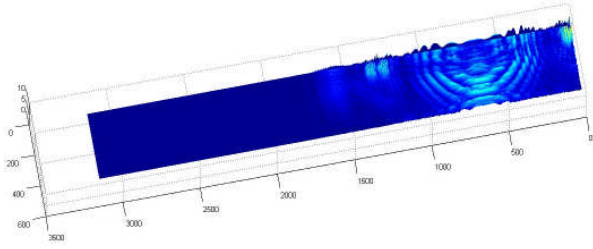


Figure 8: Velocity surface plot of EFIT simulated guided waves propagating down the length of an aluminum plate that is 1m in length, 5.8cm wide and 1.6mm thick.

### Future Work

We have presented work here that shows that the DWFT is helpful in determining the propagation and arrivals of guided wave modes. The wavelet fingerprints are binary images, so they are simple to store and straightforward to process digitally, and we can draw on the large scientific and technological literature in fingerprint and character recognition to develop computer algorithms that automatically identify features in them. By incorporating the details of the wave propagation into algorithms for inspection and structural health monitoring, we develop more informative and quantitative techniques. From here we plan to continue building up our 3D algorithms to include the corroded surface on the stringer. In this fashion we can truly model the interaction of the elastic waves with the stringers.

### Acknowledgements

I would like to thank Hasso Weiland of the Alcoa Technical center for providing the stringer samples and for helpful discussions, Don Kennamer of Oceana Sensor for providing the np3 for data collection Corey Miller for conducting some data collection, and Chris Bording for co-writing the parallel 3D simulation FORTRAN code.

<sup>1</sup> J. D. Achenbach Wave Propagation in Elastic Solids. Amsterdam: North-Holland. (1984).

- 
- <sup>2</sup> B. A. Auld, *Acoustic Fields and Waves in Solids*. Malabar, FL: Kreiger. (1990).
- <sup>3</sup> J. L. Rose, *Ultrasonic Waves in Solid Media*. Cambridge: Cambridge University Press. (1999).
- <sup>4</sup> J. L. Rose, "A Baseline and Vision of Ultrasonic Guided Wave Inspection Potential" *Journal of Pressure Vessel Technology- Transactions of the ASME* 124 (3): 273-782 (2002).
- <sup>5</sup> J. Hou, Kevin R. Leonard and M. Hinders, "Automatic Multi-mode Lamb Wave Arrival Time Extraction for Improved Tomographic Reconstruction" *Inverse Problems* 20, 1873-1888 (2004).
- <sup>6</sup> M. Hinders, J. Hou, "Dynamic Wavelet Fingerprint Identification of Ultrasound Signals" *Materials Evaluation* 60, #9 1089-1093, (2002).
- <sup>7</sup> ASTM International, "Standard Test Method for Exfoliation Corrosion Susceptibility in 2XXX and 7XXX Series Aluminum Alloys (EXCO Test)" Designation: G 34 – 01.
- <sup>8</sup> Schubert, F., Koehler, B., and Zg (2001). "Three-dimensional time domain modeling of ultrasonic wave propagation in concrete in explicit consideration of aggregates and porosity," *Journal of Computational Acoustics* 9, 1543-1560.
- <sup>9</sup> Fellingner, P., Marklein, R., Langenberg, K. J., and Klaholz, S. (1995). "NUMERICAL MODELING OF ELASTIC-WAVE PROPAGATION AND SCATTERING WITH EFIT - ELASTODYNAMIC FINITE INTEGRATION TECHNIQUE," *Wave Motion* 21, 47-66.
- <sup>10</sup> Rudd, K. E., Leonard, K. R., Bingham, J. P., and Hinders, M. K. (2007). "Simulation of guided waves in complex piping geometries using the elastodynamic finite integration technique," *Journal of the Acoustical Society of America* 121, 1449-1458.